Matter

CellPress

Article

Titanium oxide-based 1D nanofilaments, 2D sheets, and mesoporous particles: Synthesis, characterization, and ion intercalation

Hussein O. Badr, Jacob Cope, Takayuki Kono, ..., Emmanuel Castiel, Robert F. Klie, Michel W. Barsoum

hob28@drexel.edu (H.O.B.)
barsoumw@drexel.edu (M.W.B.)

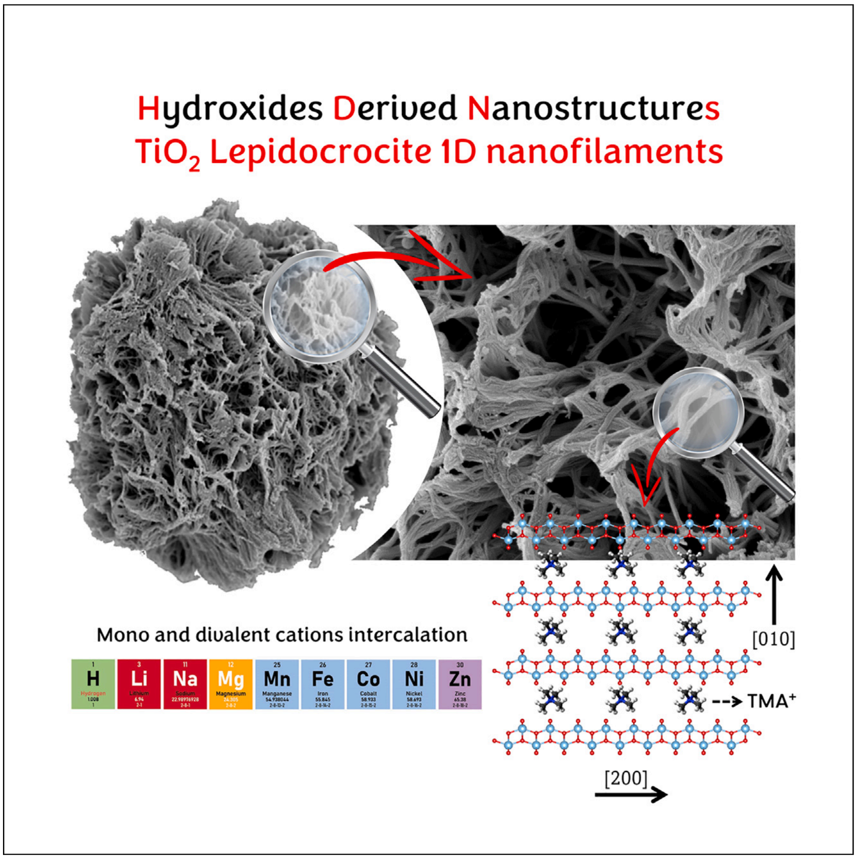

Arguably, manufacturing nanomaterials at the kilogram scale has proven more challenging than many assumed. Herein, we fully convert TiB_2 powders into lepidocrocite, TiO_2-based nanofilaments — 5 × 7 $Å^2$ in cross section that self-assemble into nanobundles ≈10–20 nm in diameter and microns long—by reacting them with tetramethylammonium hydroxides in plastic bottles at 80°C and 1 atm for 72 h. The nanobundles, in turn, self-assemble into free-flowing mesoporous particles that retain a nanomaterial's advantages without the need to de-flocculate them.

Highlights

Large-scale synthesis of lepidocrocite titania-based one-dimensional nanofilaments

Nanofilaments are 5 × 7 $Å^2$ in cross section, ≈10–20 nm long

Depending on solvent, nanobundles self-assemble into 2D sheets or mesoporous particles

Cations in the interfilamentous space are readily interchangeable

2

Benchmark

First qualification/assessment of material properties and/or performance

Badr et al., Matter 6, 3538–3554
October 4, 2023
https://doi.org/10.1016/j.matt.2023.07.022

CellPress

Matter

Article

Titanium oxide-based 1D nanofilaments, 2D sheets, and mesoporous particles: Synthesis, characterization, and ion intercalation

Hussein O. Badr,[1,*] Jacob Cope,[1] Takayuki Kono,[2] Takeshi Torita,[2] Francisco Lagunas,[3] Emmanuel Castiel,[1] Robert F. Klie,[3] and Michel W. Barsoum[1,4,*]

SUMMARY

In this work, we report on the large-scale synthesis of TiO_2-based one-dimensional (1D) nanofilaments (NFs) using a facile, bottom-up, one-pot, solution-processing synthesis protocol. Our method entails mixing TiB_2 commercial powders with tetramethylammonium-hydroxide (TMAH) in plastic bottles at 80°C for a few days under ambient pressure. The resulting lepidocrocite titania-based 1D NFs, with $\sim 5\times7$ Å^2 cross-sections self-assemble in a plethora of nanostructures that depend on solvent used for washing. In ethanol, they form mesoporous particles that are free flowing, and nearly spherical, with an average diameter in the ≈ 13 μm range. In water, they self-assemble into pseudo-two-dimensional flakes comprised of nanobundles. The formation of the NFs occurs at the TiB_2/reaction reagent interface allowing for the formation of core-shell configurations. The intercalating TMA^+ cations between the NFs can be readily exchanged with H_3O^+, Li^+, Na^+, Mg^{2+}, Mn^{2+}, Fe^{2+}, Co^{2+}, Ni^{2+}, or Zn^{2+} cations. With zeta-potential values of ≈ -50 mV, the resulting materials form quite stable colloids in water.

INTRODUCTION

Titania (TiO_2) nanostructures have been, and remain, of significant research interest due to their unique physical and chemical properties as well as their potential application in a wide range of fields including paint pigment, catalysis, photocatalysis, photoluminescence, gas sensors, and solar and fuel cells.[1–12] Among commercially available nanostructured titania, Evonik's Aeroxide TiO_2 P25 (formerly sold by Degussa), and hereafter referred to as P25, stands out. P25 synthesized via flame pyrolysis of $TiCl_4$, is attractive because of its high photocatalytic activity.[13–18] In many ways, P25 has been, and is still, considered the gold standard for TiO_2-based catalytic and photocatalytic applications. Its major drawback, however, is its cost; flame pyrolysis is a relatively expensive process. Arguably, had P25 been cheaper it would have found more applications. This is important herein because we developed a significantly cheaper process to make one-dimensional (1D) titania, which we have shown performs better than P25 in a number of applications.[19]

A schematic of our facile, one-pot, solution-reprecipitation method is shown in Figures 1A and 1B. The recipe entails reacting precursor powders with tetramethylammonium hydroxide (TMAH) aqueous solutions—in polyethylene bottles—in the 50°C to 85°C temperature range for a few days. In one case, we reacted five different Mn-containing powders, such as Mn_3O_4, Mn_2O_3, and MnB, in TMAH aqueous solutions for a few days and converted them into birnessite-based two-dimensional (2D)

PROGRESS AND POTENTIAL

Applications of titanium oxide nanostructures span over numerous fields from the paint pigment industry, to electro- and photocatalysis, to solar cells, among others. Roughly 2 years ago, we discovered a method to convert cheap and earth-abundant titanium-containing powders, such as TiC, TiN, and TiB_2, into titanium oxide-based nanofilaments (NFs) 10– 30 nm long with cross sections that are in the sub-nanometer scale. Our process is scalable and simple: we react precursors with tetramethylammonium hydroxides in plastic bottles at temperatures <100°C and 1 atm for tens of hours. Herein, we report on how these NFs can self-assemble to form mesoporous particles—in the micrometer range—on the kilogram scale. We also show how the cations between the NFs can be easily exchanged. The implications of this discovery in the field of nanomaterials cannot be overemphasized as now one can prepare nanostructures in a home-kitchen setup.

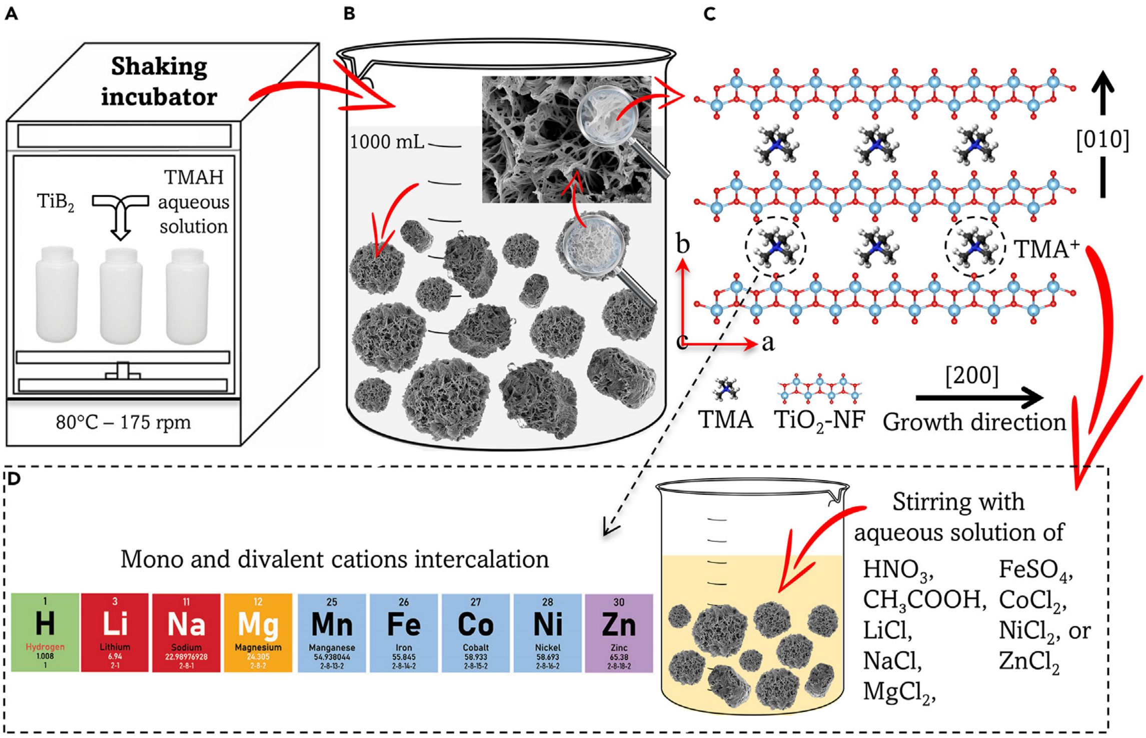

Figure 1. Scalable synthesis of NFs-based mesoporous particles

(A) Schematic of temperature-controlled shaking incubator used to convert TiB$_2$ precursor powder into NFs-based mesoporous particles.

(B) Washing procedure followed to remove any unreacted TMAH.

(C) DFT-generated lepidocrocite structure showing ribbons two Ti-atoms thick growing along [100] and stacking along [010] (viz., the *a* and *b* crystallographic directions, respectively).

(D) Various cations (both mono- and divalent) intercalated in the interfilamentous gallery.

sheets with thicknesses of 2$\pm$0.4 nm that were $\approx$ 200 nm across.[20] Compared to other bottom-up approaches in the literature,[21–23] our 2D birnessite sheets were remarkably crystalline. They, in turn, demonstrated enhanced electrochemical reactivity for both reversible O$_2$ electrocatalysis and supercapacitor applications.[20,24] In a more recent article, we showed that it is possible to synthesize the same flakes with using aqueous solutions of tetraethylammonium hydroxide (TEAH) and tetrabutylammonium hydroxide (TBAH).[25]

Following the same protocol, we immersed FeB powders in alkaline aqueous solutions (TMAH, TBAH, or potassium hydroxide [KOH]) and sythesized ferromagnetic Fe$_3$O$_4$ nanoparticles with an average particle size of $\sim$15 nm.[26]

In another example, more germane to this work, we converted cheap, earth-abundant, water-insoluble Ti-bearing precursors including TiC, TiN, and TiB$_2$ into 1D nanofilaments (NFs).[27] The recipe is similar to that used to make birnessite flakes and entails reacting Ti-bearing precursor powders with, again, TMAH aqueous solutions—in polyethylene bottles—in the 50°C to 85°C temperature range for a few days. In our original report,[27] we concluded that the 1D NFs structure is anatase based because the Raman spectra were those of anatase. In more recent work—using a combination of high-resolution scanning transmission electron microscopy (HR-STEM), selected area diffraction (SAD), and Raman spectroscopy—we concluded that the 1D NFs crystallize in a lepidocrocite-type TiO$_2$-based structure (Figure 1C).[28] Henceforth, these lepidocrocite 1D NFs will be referred to as 1DL

[1]Department of Material Science and Engineering, Drexel University, Philadelphia, PA, USA

[2]Murata Manufacturing Co., Ltd, Nagaokakyo-shi, Kyoto, Japan

[3]Department of Physics, University of Illinois at Chicago, Chicago, IL 60607, USA

[4]Lead contact

*Correspondence: hob28@drexel.edu (H.O.B.), barsoumw@drexel.edu (M.W.B.)

https://doi.org/10.1016/j.matt.2023.07.022

NFs. In retrospect, using a laser, at full power, to acquire the Raman spectra resulted in a lepidocrocite to anatase phase transformation.[28] The cross sections of our 1DL NFs are ≈ 5×7 Å^2.[28] The extreme size led us to conclude that a quantum size effect was responsible for the record band gap energy, E_g of ≈ 4eV measured, for this bottom-up-processed, titania-based material.[27]

At this time, we concluded several studies of our 1DLs, showing them to be unique and better performing than P25. Very recently, we published the results of a careful examination of the electronic structure of our 1DLs and showed them to be quite different than P25.[29] In another paper, we showed that the photochemical hydrogen production rates, when exposed to the equivalent of two suns, were about an order of magnitude higher than P25 tested under identical conditions.[19] In the field of water purification, we showed that our 1DLs can adsorb record values of uranium (U^{4+}), rendering water contaminated by this actinide potable.[30] Furthermore, composites of our 1DLs with a repairable, dynamic, covalent thiol-yne network resulted in almost 50-times increase in the modulus at a 60 wt % filler when compared to pristine polymer.[31]

In our first report, after reaction and washing with ethanol (EtOH) to ≈ pH 7 and then washing with water, pseudo-2D (p-2D) flakes were produced upon filtration.[27] The reason we refer to them as pseudo is because the flakes—composed of 1DL NFs—are only apparently 2D. In a more recent paper, we showed that these p-2D flakes are present in the colloid, even at short reaction times.[32] It follows that water exerts a strong driving force aligning the 1DLs normal to their [100] growth direction. This self-alignment first leads to the formation of nanobundles and μ-fibers that, in turn, self-align into p-2D flakes.[32] We note in passing that the p-2D sheets are, for the most part, poorly crystalline. The most important conclusion—reinforced herein—reached, however, is that, regardless of the experimental conditions or final morphologies, the 1DL NFs remain the essential building blocks.

In this work, we show that if the 1DL NFs are dried while in ethanol (i.e., without dispersing in water), they form spherical, mesoporous particles (MPPs) with diameters that are comparable to those of the precursor powder. In this work, we (1) report on large-scale synthesis (100 g batches) of MPPs that are composed of 1DL NFs; (2) shed light on the mechanisms that lead to MPPs formation, (3) show that, as in other layered titanates,[3,33] the space between the NFs is eminently ion exchangeable (to that effect, we can readily replace the tetramethylammonium (TMA^+) cations present after the reaction stage by H^+, Li^+, Na^+, Mg^{2+}, Mn^{2+}, Fe^{2+}, Ni^{2+}, Co^{2+}, or Zn^{2+} cations, and (4) measure the surface charges and hydrodynamic radii of MPPs intercalated with TMA^+ or Li^+ ions.

The starting precursor chosen is TiB_2 because, preliminary results have shown that compared to TiC and TiN, it is the most reactive. A large batch of TiB_2 powders can be almost fully converted to 1DLs in ≈ 3 days at 80°C.

RESULTS AND DISCUSSION

In our previous work,[27] the precursors were reacted with TMAH aqueous solutions using hot plates and magnetic stirrers. To prepare batches as large as 100 g, we used a temperature-controlled shaking incubator. The experimental details can be found in the experimental procedure section below. In brief, we shake 100 g of TiB_2 commercial powders with ~1 L of a 25 wt % TMAH aqueous solution at 80°C for 1 to 5 days in a temperature-controlled shaking incubator (Figure 1A). In one set of experiments, the resulting powders were washed with EtOH multiple times using an overhead mixer, until the pH was ~7 (Figure 1B), before they were left to dry at 50°C overnight in open air.

Preliminary results indicated that when the EtOH-washed samples were placed in water, the MPPs did not retain their morphology. However, they did if the TMA^+ cations were replaced with Li^+. To explore this idea, in one set of experiments, EtOH-washed powders were stirred—while wet—in aqueous salt solutions of 0.5 M LiCl, 5 M LiCl, 0.5 M NaCl, or 5 M NaCl (Figure 1D). The powders were then rinsed with deionized (DI) water a few times to remove any residual salts before drying similarly at 50°C in open air.

To assess the capability of intercalating various mono- and divalent cations between the NFs, both the EtOH- and the EtOH/LiCl-washed powders were further treated in one of the following aqueous solutions (Figure 1D): (1) 0.1 M nitric acid (HNO_3) or 0.5 M acetic acid, or (2) 0.02 M aqueous solution of one of the following salts: $MgCl_2$, $MnCl_2$, $FeSO_4$, $CoCl_2$, $NiCl_2$, or $ZnCl_2$. In all cases, after being immersed in the salt solutions, the powders were washed a few times with DI water and dried at 50°C in open air for 24 h.

Characterization of 1DL NFs

Before proceeding further, it is important to understand the X-ray diffraction (XRD) signature of our 1DL NFs. The reaction time dependencies of the XRD patterns—on a semi log scale—are shown in Figure 2A. In a typical 1DL XRD pattern (Figure 2A), three types of peaks exist.[28] The first are due to unreacted precursor—TiB_2 in this case—denoted by dashed black vertical dashed lines in Figure 2A. These are useful in that they can be used as internal standards. The second, 0k0 peaks and higher at low 2θ angles denoted by asterisks in Figure 2A,reflect the *d*-spacing values between the NFs stacked along the *b*-direction. Previously, we indexed these peaks as 001 peaks, which more recent work has shown to be incorrect.[28] Like in other 2D materials, such as MXenes[34,35] and others,[3,33] these peak locations are strong functions of what cations are intercalated between them.[28] Crucially, here the distance is not between flakes but between NFs. Based on the results shown in Figure 2A, it is clear that, after the first day, the *d*-spacings are no longer functions of reaction time.

Based on d-spacing values, careful analysis of our XRD patterns and previous work,[9] we index the peak at ~26° 2θ as 130 (denoted by gray band in Figure 2A). This peak is a weak function of the nature of cations between the NFs.[28] The small peak to its left is 110. The last, and most fundamental peaks, are those at 2θ values of ~ 48° and 62°—denoted by red bands in Figure 2A—indexed as 200 and 002 of the lepidocrocite titania structure, respectively. These peaks are important because they are crystallographic in nature and should—as confirmed herein—be totally independent of what cations surround the NFs. It is from these 2θ values that we obtain the *a*- and *c*-lattice parameters of lepidocrocite, viz. 3.78 and 2.96 Å, that match previous work.[36,37] Note, in our assignments of the various peaks, which is different from our previous work, we followed the indexing used previously.[9,37,38]

As just noted, Figure 2A shows the time dependencies of the XRD patterns of the TiB_2 precursor powder (top pattern in Figure 2A) as well as those reacted at 80°C for 1–5 days, shown from top to bottom in Figure 2A. As the reaction times increased from 1 to 3 days, the intensity of the TiB_2 diffraction peaks gradually decreased, whereas the 1DL ones became dominant. The latter is recognized by a set of characteristic non-0k0 reflections (highlighted by light blue, gray, and red bands in Figure 2A and the low-angle 020 diffraction peak at 9° 2θ (and its higher order 040 peak). From the latter, the distance between the 1DL NFs is calculated to be

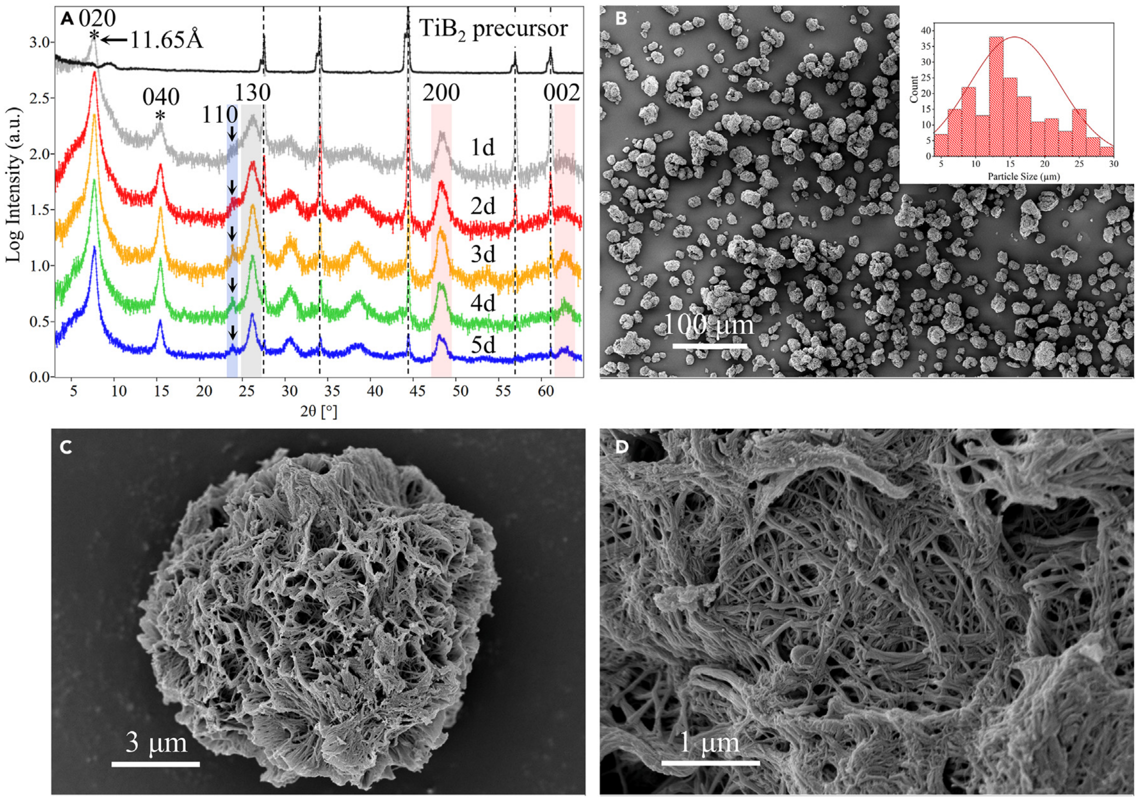

Figure 2. XRD and SEM characterization of 1DL-based mesoporous particles prepared by shaking TiB_2 powders in TMAH aqueous solution at 80°C and ethanol washing

(A) XRD patterns—on a semi log scale—of TiB_2 precursor powder (top black curve) as well as samples reacted for 1–5 days then washed with ethanol before drying at 50°C in air overnight. Peaks at ≈ 23.7°, 26°, 48°, and 62° 2θ correspond to 110, 130, 200, and 002 planes, respectively, of lepidocrocite titania. The first two 0k0 peaks, 020 and 040, are denoted by asterisks. Vertical dashed black lines denote TiB_2 diffraction peaks. Vertical black arrows, in blue band, denote 110 lepidocrocite peaks at ≈ 23.7°. Grey band denotes 130 peak, and red bands outline 200 and 002 peaks.

(B–D) SEM micrographs— at various magnifications—of mesoporous particles after 5 days of reaction. Inset in (B) shows MPP's size distribution obtained using ImageJ from SEM micrograph. Figures S1–S3 show more SEM images.

11.65 Å. These results suggest that, after 3 days, the conversion of the precursors into 1DL powders is complete. However, to minimize the fraction of unreacted precursor, we ran the reaction for 5 days. All characterizations were carried out on powders reacted for 5 days (blue pattern in Figure 2A).

Scanning electron microscope (SEM) micrographs of typical MPPs after EtOH washing to pH 7 are shown in Figures 2B–2D. At the millimeter scale, the powders appeared to be well dispersed with little to no aggregation observed (Figure 2B). At higher magnification, the MPPs are porous, mostly spherical, with an average size of ~13 μm (inset in Figure 2B) and composed of entangled 1DL NF bundles (Figures 2C and 2D). Notably, the shape and size of the MPPs are quite consistent over 50 different batches prepared and characterized to date. Other micrographs are shown in Figures S1–S3. To summarize this section: after washing with EtOH, the 1DL NFs self-assemble into separate, non-agglomerated, *free-flowing* MPPs, in the 5 to 30 μm particle diameter size range (Figure 2B and inset).

To better understand the MPP structure, we imaged them using a high-resolution scanning transmission electron microscope (HR-STEM) (Figures 3A–3C). If one assumes that the fiber bundle shown in Figure 3A is a single MPP, then its diameter is about 1 μm.

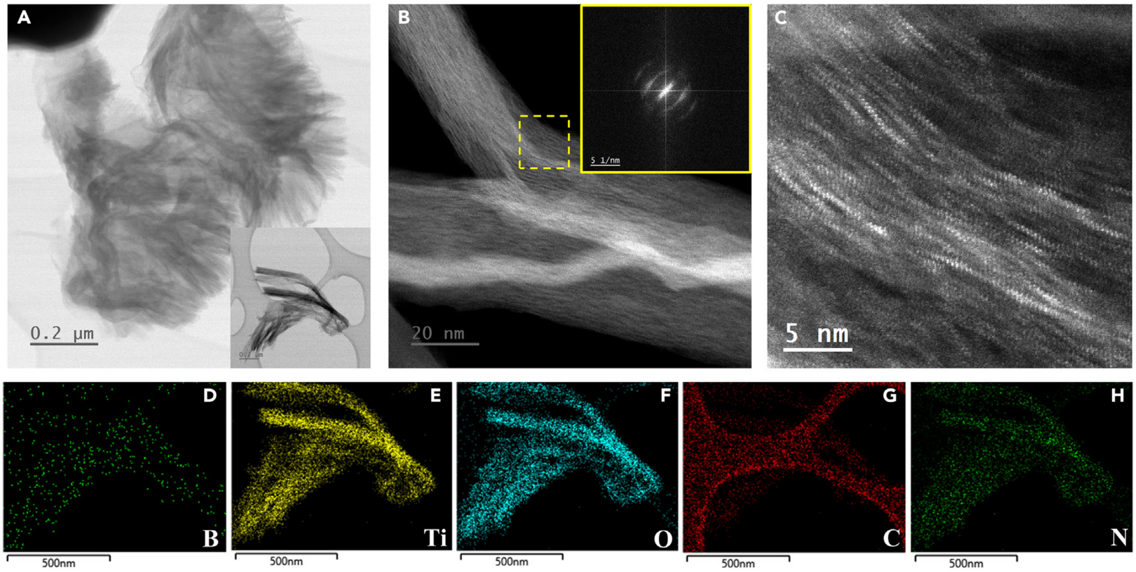

Figure 3. STEM imaging and elemental mapping of 1DL-based MPP derived from TiB_2 shaken in TMAH aqueous solution at 80°C for 5 days, rinsed with ethanol, then dried at 50°C overnight in open air

(A) Typical STEM image of mesoporous particle > 1 µm in lateral size.

(B and C) LAADF STEM micrographs—at various magnifications—of bundles of 1DL NFs oriented along the fiber axis. Inset in (B) shows FFT produced from area bounded by dashed yellow square.

(D–H) EDS elemental maps of B, Ti, O, C, and N, respectively, of particle shown in inset in (A).

At higher magnifications, it is obvious that the bundle is, in turn, composed of a multitude of 1DL NFs (Figures 3B and 3C). Importantly, a low-angle annular dark field (LAADF) image (Figure 3C) shows that the building unit remains NFs, two Ti-atoms wide, with a zigzag pattern identical to that previously imaged.[28] Fast Fourier transform (FFT) pattern of the bundles (inset in Figure 3B) resulted in two main arcs—confirming the 1D nature of our NFs—with *d*-spacings corresponding to XRD peaks at 2θ values of ~26° and ~48° (gray and red dashed bands in Figure 2A). This result is in total agreement with our previous work.[27,28] Also in accord with our recent work, the arcs bisect the [100] growth direction. For a detailed discussion on the structure of the 1DL NFs, the interested reader can consult a recently published article.[28]

Turning to the composition of the 1DL bundles, we obtained scanning transmission electron microscope (STEM) micrographs and energy-dispersive X-ray spectroscopy (EDS) maps of the MPP shown in inset in Figure 3A. Only trace amounts of B (<1%) were detected (Figure 3D), which is consistent with the almost-complete conversion of TiB_2 into 1DL NFs and the effectiveness of our process in washing out any B-containing reaction products. Importantly, from a scaling point of view, these powders were neither centrifuged nor filtered. Note the uniform distribution of Ti and O atoms shown in Figures 3E and 3F, respectively. The calculated atomic percentage ratios of Ti and O are 24.5% and 49.5% respectively, consistent with a TiO_2 stoichiometry. The lacey carbon support is visible in the C map (Figure 3G) and overshadows the C in the 1DL. The uniform distribution of N on the MPPs supports the fact that some TMA^+ ions remain intercalated between the NFs (Figure 3H). It is difficult to quantify the N amount present because of the large overlap between the N *K*- and the Ti *L*-edges.

To solve this problem and obtain a better handle on the C content, we acquired electron energy-loss spectroscopy (EELS) spectra where the Ti and N peaks are

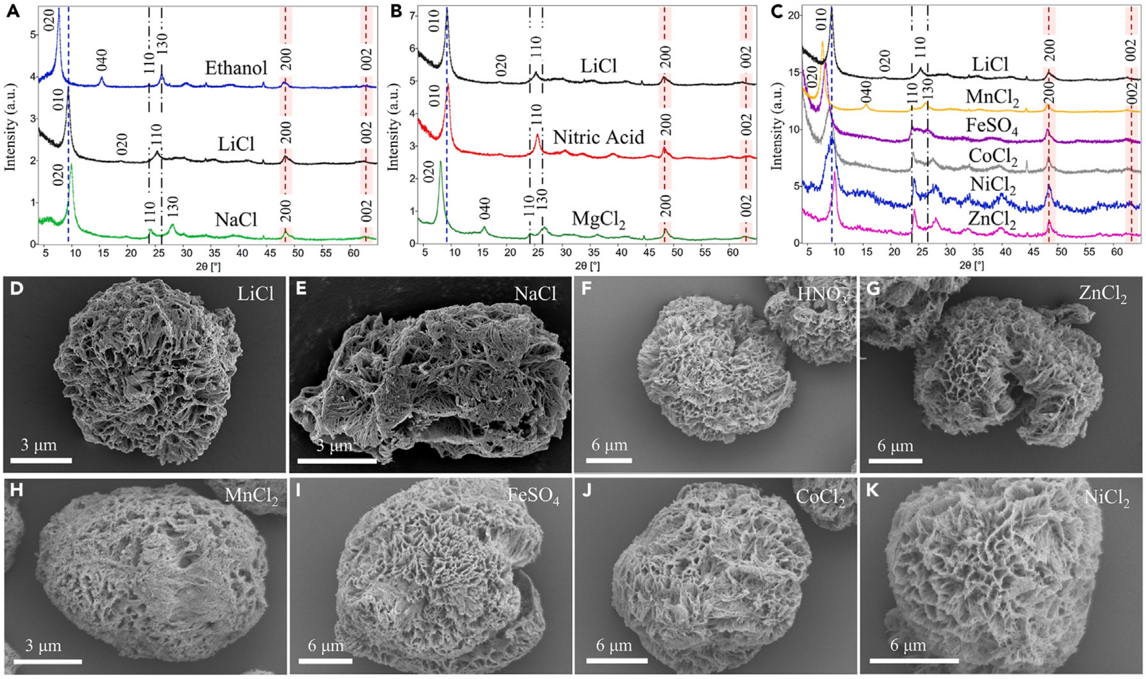

Figure 4. Characterization of 1DL-based mesoporous particles intercalated with various mono- and divalent cations

(A–C) Partially indexed XRD patterns. Consistent with titania-based lepidocrocite literature, when the lowest angle peak is designated 010, the 25 peak is 110; if first peak is 020, then a 130 peak emerges. (D–K) SEM micrographs for MPPs prepared by shaking TiB_2 precursor powder in TMAH solution at 80°C for 5 days, washing with solvent/aqueous solutions of salts labeled on the panels, and drying at 50°C in open air.

easily distinguishable, and the elemental compositions can be calculated using Hartree-Slater cross-section models. To further reduce the contribution of surface hydrocarbons, we *in situ* cooled the sample using a liquid nitrogen cold stage. The elemental maps derived from core loss spectra (Figure S4) show Ti and O concentrations, again, consistent with a TiO_2 stoichiometry. The C to N ratio is 4.5, which is consistent with the expected ratio of 4 for TMA cations.

Cationic exchange of 1DL NFs

In our first report on these 1DL NFs, we established that we could readily ion exchange the TMA^+ cations—present after EtOH washing to pH ≈ 7—with Li^+.[27] Here we show that the Li^+ cations can, in turn, be replaced by the following cations: H^+, Na^+, Mg^{2+}, Mn^{2+}, Fe^{2+}, Co^{2+}, Ni^{2+}, and Zn^{2+}. The XRD patterns after ion exchange are plotted in Figures 4A–4C. Typical SEM micrographs of the MPPs are shown in Figures 4D–4K. Figures S5A–S5C plot the same data shown in Figures 4A–4C, respectively, but on a semi-log scale.

As noted in the experimental procedures section, after ion exchange, all powders were rinsed with DI water multiple times and allowed to dry at 50°C in open air before any further characterization. In all cases, the absence of all but 1DL XRD peaks (Figures 4A–4C and S5A–S5C) confirm that we successfully eliminated most of the unreacted salts and unwanted reaction products. This also implies that the unwanted reaction products are water soluble.

After EtOH washing (blue patterns in Figures 4A and S5A), the first peak at ~7.5° 2θ, corresponds to a 020 reflection for which the d ~11.65 Å. This *d*-spacing is a measure of the thicknesses of the NFs along the *b*-direction together with any intercalated ions and/or water.[39–41] Since we know from density functional theory (DFT) calculations that the thickness of one NF along the *b*-direction is ≈ 5 Å, it follows that the TMA^+ and H_2O thickness is ≈ 6.5 Å, which is reasonable and in good agreement with other literature reports.[40,41]

After washing with LiCl or NaCl aqueous solutions (black and green patterns, respectively, in Figures 4A and S5A), the *d*-spacing shrinks to 9.5 and 9.0 Å, confirming that the TMA^+ ions were successfully exchanged with Li^+ or Na^+ ions, respectively. The slightly higher *d*-spacing associated with Li^+-intercalated powders, as compared to Na^+, probably reflects the former's slightly larger hydration shell. Again, assuming the thickness of one NF along the *b*-direction is ≈ 5 Å, it follows that the $Li^+ + H_2O$ and $Na^+ + H_2O$ thicknesses are 4.5 and 4.0 Å, respectively, again in decent agreement with literature results.[36,42,43]

Figure 4B shows XRD patterns for powders that were first washed with LiCl aqueous solution and *then* treated in HNO_3 or $MgCl_2$ aqueous solutions. The XRD patterns for the remaining cations are plotted in Figure 4C. The initial *d*-spacing was ≈9.5 Å (top black pattern in Figures 4B and 4C) for Li^+-intercalated NFs. When stirred in 0.1 M HNO_3, the 9.5 Å-peak slightly shifted to ≈ 9.3 Å (red pattern in Figure 4B), suggesting the successful intercalation of hydronium ions between the NFs. The obtained *d*-spacing value is in a good agreement with other reports in the literature for protonated lepidocrocite titanates.[3,9,38] Likewise, stirring the Li^+-intercalated NFs in a 0.02 M $MgCl_2$ solution (green pattern in Figure 4B) resulted in a *d*-spacing expansion from 9.5 to 10.8 Å, which we take as evidence for the exchange of Li^+ ions with Mg^{2+}.

The situation is quite similar for other divalent cations (Mn^{2+}, Fe^{2+}, etc.). Cationic exchange between Li^+, on one hand, and Mn^{2+}, Fe^{2+}, Co^{2+}, Ni^{2+}, and Zn^{2+} on the other hand, occurs when LiCl-washed powders were further treated in 0.02 M aqueous solutions of the targeted cations. As shown in Figure 4C, the resulting *d*-spacings after cationic exchange are 11.4, 10.7, 9.8, 9.4, and 8.9 Å for Mn^{2+}, Fe^{2+}-, Co^{2+}-, Ni^{2+}-, and Zn^{2+}-intercalated 1DL NFs, respectively.

Interestingly, when EtOH-washed powders were *directly*—i.e., without first exchanging the TMA^+ with Li^+—immersed in HNO_3, $CoCl_2$, or $NiCl_2$ aqueous solutions for 24 h or longer, the low-angle peaks vanish (Figure S6A), implying that any order along the *b*-stacking direction was destroyed. The only remaining peaks were the three reflections at 2θ values of ≈ 26°, ≈ 48°, and ≈ 62° (red bands in Figure S6A). An SEM micrograph of an $NiCl_2$-washed sample (Figure S6B) confirms a change in the MPPs' morphology into nanometer-sized, slightly porous agglomerates.

To summarize this section, the interfilamentous space between the 1DL NFs is quite readily exchangeable with monovalent (H_3O^+, Li^+, and Na^+) and divalent (Mg^{2+}, Mn^{2+}, Fe^{2+}, Co^{2+}, Ni^{2+}, and Zn^{2+}) cations. The corresponding XRD patterns clearly demonstrated the successful intercalation of these cations by the slight shifting of low-angle (<10°) 2θ peaks. It is crucial to note here that the peaks located at ~ 48° and 62° 2θ (red dashed lines/bands in Figures 4A–4C and S5A–S5C) *perfectly* lined up in *all* cases regardless of the nature of the intercalants. This result indirectly confirms the correctness of assigning these peaks to the 1DL backbone (see below).[9,37]

Surface charge and hydrodynamic size of NF agglomerates

A motivation of this work was to investigate the surface charge and aggregation behavior of the prepared NFs and NFs-based MPPs intercalated with TMA^+ or Li^+

Table 1. ζ-potentials and average hydrodynamic diameters, d_H, measured as a function of washing media; washing order is shown in two left-hand columns

		ζ-potentials (mV)		d_H (nm)	
Washing solution		Average	SD	Average	SD
EtOH		−5	1.5	1,110	45
EtOH ➤ H_2O		−53	10	2,071	850
EtOH➤LiCl➤H_2O➤	0.05 M LiCl	−33	1.3	640	390
	0.5 M LiCl	−31	1.9	414	80
	5.0 M LiCl	−28	0.5	168	50

cations. To that effect, we measured the zeta (ζ) potentials and hydrodynamic diameters (d_H) of the powders, once after EtOH washing and again after washing with LiCl aqueous solutions. Note that, apart from the first sample (top row in Table 1), which was washed and measured in EtOH, all other samples were washed with solvents/solution listed in the first column in Table 1, then dispersed in DI water for ζ potential and d_H measurements. All measurements were repeated three times; results are averaged (see Figure 5) and summarized in Table 1.

When the solvent was EtOH, the ζ potential of the MPPs was -5 ± 1.5 mV, which explains colloid instability in this solvent; the MPPs settled to the bottom of the container (Figure S7A) and only particles/entities with d_H of ~0.1 μm (right axis in Figure 5) remained suspended. When the MPPs were dispersed in DI water, a ζ potential of $\sim -53 \pm 10$ mV is recorded, which, in turn, resulted in highly stable colloidal suspensions (see Figure S7B). The high surface charge stabilized agglomerates of 1DL NFs as large as 2 ± 0.8 μm (right axis in Figure 5). Notably, the size of these aggregates is a function of colloidal concentration. In previous work,[27] we showed that single NFs (with thickness of ~1.5 nm) can be obtained by diluting a colloidal suspension 500× (see atomic force microscopy [AFM] scans in Figures S8A and S8B for drop-cast samples before and after dilution, respectively). Upon washing the MPPs—right after EtOH washing—with LiCl solutions, the ζ-potential values were reduced from -53 ± 10 mV in DI water to -33.0 ± 1.3 mV in 0.05 M LiCl solution (Figure 5; Table 1). As the molarity of the LiCl solution increased to 5 M, the ζ potentials dropped slightly to $\approx -28.0 \pm 0.5$ mV (Figure 5; Table 1).

Notably, when the MPPs (after washing with ethanol to neutral) were dried at 50°C and then redispersed in DI water, there was a noticeable increase in the pH up to values of ~10, which can be caused by the uptake of protons by O^- and/or OH^- surface terminations. To that effect, Yuan et al. observed a similar increase in pH of a solution by a protonated layered titanate and suggested the formation of an extra hydration layer.[38] That was supported by the appearance of an extra low-angle peak with a spacing of 11.65 Å in addition to the original 9.2 Å reflections.[38] In our case, however, we did not observe any changes in the low-angle peaks, suggesting that the surface oxygen atoms are hydroxylated through protonation.[9]

To summarize, after neutralization in EtOH, the ζ potential was slightly negative and most of the MPPs settled (Figure S7C). Only aggregates <1.4 μm in size were suspended in the EtOH (Figure 5). Upon washing with water, at $\approx -50 \pm 10$ mV, the ζ potential was quite negative, which explains the colloidal stability in water.

The major drop in surface charge from DI water to 0.05 M LiCl solution basically corresponds to Li^+ ions' electrostatic adsorption on the NFs' negatively charged

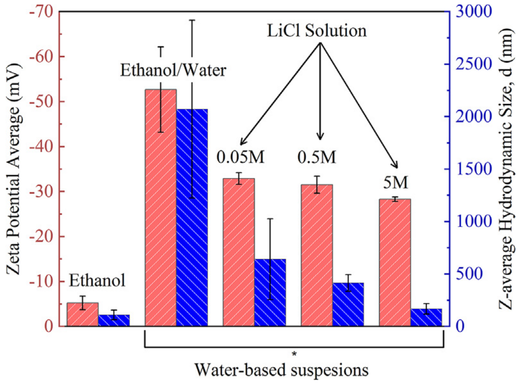

Figure 5. Zeta potential (left y axis) and average hydrodynamic size (right y axis) of TiB_2-derived samples shaken in TMAH at 80°C for 5 days then washed with solvents/solutions as labeled. Error bars represent one standard deviation. In absence of water, suspension is unstable.

surfaces, which in turn resulted in a decrease in the electrical double layer and a consequent drop in the repulsive electrostatic interaction between the NFs. The subsequent drop in surface charge as the molarity increased from 0.05 M to 5 M (Figure 5; Table 1) is further evidence for the decrease in the thickness of the diffuse layer of the 1DL NFs as the ionic strength increased.[44]

Thermal stability of 1DL NFs

The thermal stabilities of our MPPs were explored using TGA in Ar up to 800°C of NFs intercalated with TMA^+, Li^+, or Na^+. All powders were dried at 50°C in open air for 24 h prior to the TGA experiments. The TGA results were different for EtOH- and salt-washed samples shown in Figure S9A. These results are reminiscent of our previous work on TiC-derived samples in that the EtOH-washed samples lost more weight than their salt-washed counterparts.[27] The salt-treated powders lose weight until ≈ 250°C, before leveling off. The weight change at that temperature is predominantly due to loss of H_2O.[27] Washing with LiCl solution results in a slightly higher (18%) weight loss than washing with NaCl (15%) (Figure S9A).

Heating EtOH-washed, TMA^+-intercalated NFs to 200°C, resulted in a ≈ 15% mass loss, probably due to residual EtOH solvent from washing (Figure S9A). Upon further heating, at ≈ 350°C, there was another mass drop of ≈ 15%, which is probably due to the loss of hydration layers and intercalated TMA cations between the NFs (Figure S9A). Heating to 200°C does not change the XRD patterns (Figure S9B). When heated to 800°C, however, the resulting structure is anatase, with small amounts of rutile (green pattern in Figure S9B), and the mesoporous morphology, at the micrometer scale, appears to be retained (Figures S10D and S10E). However, at higher magnifications (Figure S10F), it is obvious that some of the NFs started spheroidizing and coarsening when compared to those heated only up to 200 °C (Figure S10C).

Heating the LiCl-washed MPPs led to one mass loss event of ≈ 17 wt % up to ≈ 200°C (Figure S9A), which most likely corresponds to the loss of hydration layers associated with Li cations and/or dehydroxylation. The case for the NaCl-washed MPPs is quite similar, in that the observed the mass loss, up to ≈ 200°C, was about 14 wt % (Figure S9A). The higher mass loss for the LiCl-washed samples (17%) suggests that the number of water molecules associated with the Li ions is slightly higher than that of Na, where the weight loss is ≈ 15%. When the powders were further heated to 800°C, no further weight loss was observed.

XRD patterns, however, show that the Li^+-intercalated NFs transformed to a mixture of rutile and lithium titanate ($Li_2Ti_2O_4$; green pattern in Figure S9C). After calcination at 800°C, the Na^+-intercalated NFs converted to a mixture of rutile and sodium titanate ($Na_2Ti_6O_{13}$), with some traces of anatase TiO_2 (red pattern in Figure S9C). The obtained mixtures of TiO_2 and $Li_2Ti_2O_4$ or TiO_2 and $Na_2Ti_6O_{13}$ after TGA are in line with other reports in the literature of titanate calcination under inert atmospheres.[42] It is also in line with the instability of our 1DL NFs under the laser light of our Raman spectrometer.[28]

1DL NF morphologies, formation mechanism, and self-assembly

The importance of this work lies in the light it sheds on the correctness of our 1DL structure, where the reaction occurs, and its nature.

Correctness of model

If our 1DL model (Figure 1C) is correct, then the 200 and 002 peaks, observed ~ 48° and 62° 2θ, respectively, should be *independent* of the nature of the cations surrounding the 1DLs. Gratifyingly, that is the case (red vertical bands in Figures 2A, 4A–4C, and S5A–S5C). In contradistinction, the 110 and 130 peaks, located at ~ 23.7° and 26° 2θ, respectively, for TMA^+-intercalated NFs, should weakly depend on the nature of the surrounding cations as observed (see vertical dashed/dotted black lines at 23.7° and 26° 2θ in Figures 4A–4C and in Figures S5A–S5C). At this juncture, it is acknowledged that the changes in the XRD patterns that occur in the vicinity of the 110 and 130 pair of refections must correleate to the configurations of the host layers of lepidocrocite and their interaction with intercalants. More work currenly ongoing to better understand these structural changes, beyond the scope of this paper, is needed. For example, at this time, we cannot rule out the formation of other titanate phases such as di-titanate, tri-titanate, and tetra-titanate previouly reported in the literature.[45,46]

Where the reaction occurs and its nature

In our first report, we presented microstructural evidence suggesting that the reaction occurred at the precursor surface.[27] Herein, we confirm this important conclusion as follows. The XRD patterns of samples reacted for 1 to 5 days, shown in Figure 2A, make it clear that, at early times, strong TiB_2 peaks (dashed black lines in Figure 2A) are present. The corresponding SEM micrographs (Figures 6 and S11) clearly show that, regardless of reaction times, and at all magnifications, the MPPs surfaces appear to be *identical*. This is a crucially important observation because it indicates the TiB_2 to 1DL transformation starts at the surface and moves inward into a central core with time. This also suggests that, at least initially, the reaction must be surface reaction rate controlled (see Figure S12). Figure 7A is a schematic of what we imagine is happening at the interface. First, Ti atoms are released into the reaction medium, at which time they convert to TiO_6 octahedra. The latter then insert themselves between the receding substrate and the 1DL growing away from it. The implications of this conclusion are important because, in principle, it allows for the formation of core-shell configurations.

One of the major disadvantages of working with nanomaterials in general, and nanoparticles in particular, is that after, typically, considerable effort goes into making them, they aggregate, and more processing is needed to disaggregate them, which in turn can introduce unwanted chemicals and contaminants. It follows that the fact that our MPPs are *free flowing* could be paradigm shifting in that we can now have many of the advantages of reduced dimensions without their downside.

Note that the fact that the NFs nucleate on the surface of our precursors may also explain why these 1DL NFs were not discovered earlier. In most sol-gel work to

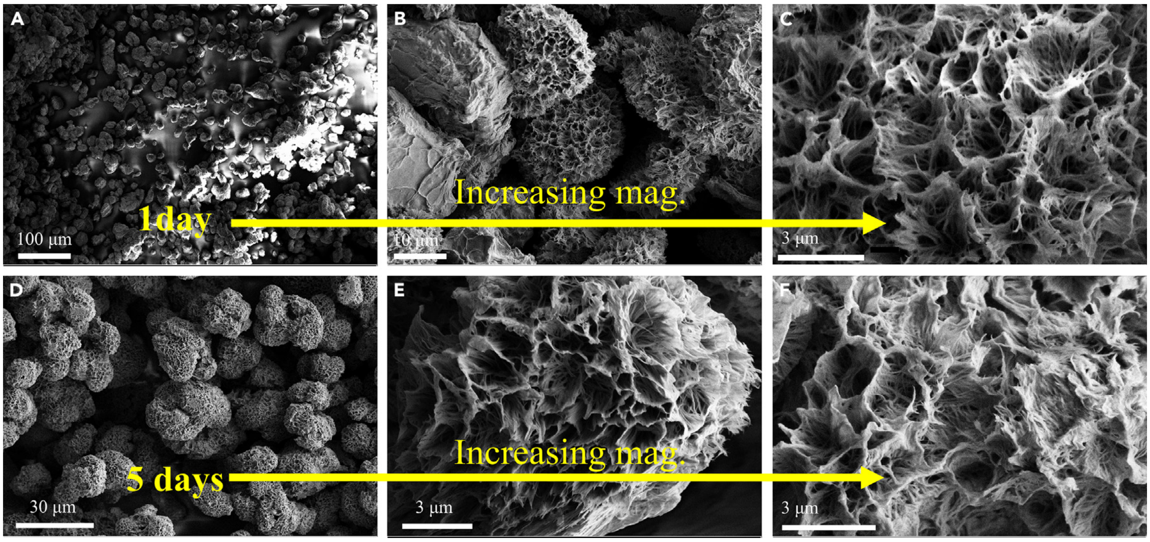

Figure 6. Reaction time dependencies of the MPP surface morphologies

SEM micrographs, at various magnifications, of samples after reaction for (A–C) 1 day, and (D–F) 5 days. Samples were reacted in TMAH at 80°C then washed with ethanol before drying at 50°C in ambient air. Micrographs after reaction for 2, 3, and 4 days are shown in Figure S11 and are no different than the ones shown here.

date, the starting point is a water-soluble Ti source. We speculate that having the reaction nucleate on a solid surface allows the NFs to only grow in one dimension. More work is needed here. What is unmistakable, however, is that a form of Ostwald ripening is occurring in our microstructures. The primary particle size of our initial TiB_2 is in the 5 µm range, with few particles over 10 µm in size.[32] As shown in inset in Figure 2B, the final sizes of the MPPs are significantly larger. This result not only confirms Ostwald ripening as a mechanism but, as importantly, clearly demonstrates that our final product, 1DL NFs, can dissolve and reprecipitate in our reaction medium.

Lastly, we would like to summarize the observations made in this work. If MPPs are desired, then the system should *not* be exposed to water (top row in Figure 7B). If the MPPs are to be ultimately used in water while maintaining their morphology, then the TMA^+ cations need to be repalced by Li^+ (second row in Figure 7B). If the MPPs are placed in water, they tend to dissaggregate and self-assemble into quasi-2D flakes (bottom right in Figure 7B). Incidentally, the same quasi-2D morphology is readily obtained if, after bringing the pH to neutral in ethanol, water is introduced.

Conclusions

In summary, we report on a truly large-scale synthesis of TiO_2-based sub-nanometer 1D structures following a facile solution-precipitation method at ambient pressures and at temperatures <100°C. Our method entails shaking water-insoluble, relatively cheap, and commercial Ti-containing powder (TiB_2 in this case) in TMAH aqueous solutions in plastic bottles at 80°C for 1–5 days. The resulting powders, washed with EtOH using an overhead mixer and a beaker before they were left to dry at 50°C in open air. This resulted in mesoporous particles with an average diameter of 13 mm and a sponge-like surface morphology. The MPPs' morphology is only stable in water if the TMA^+ cations are replaced by Li^+. In the absence of ion exchange, the MPPs transform into quasi-2D layers that are, in turn, also comprised of NFs.

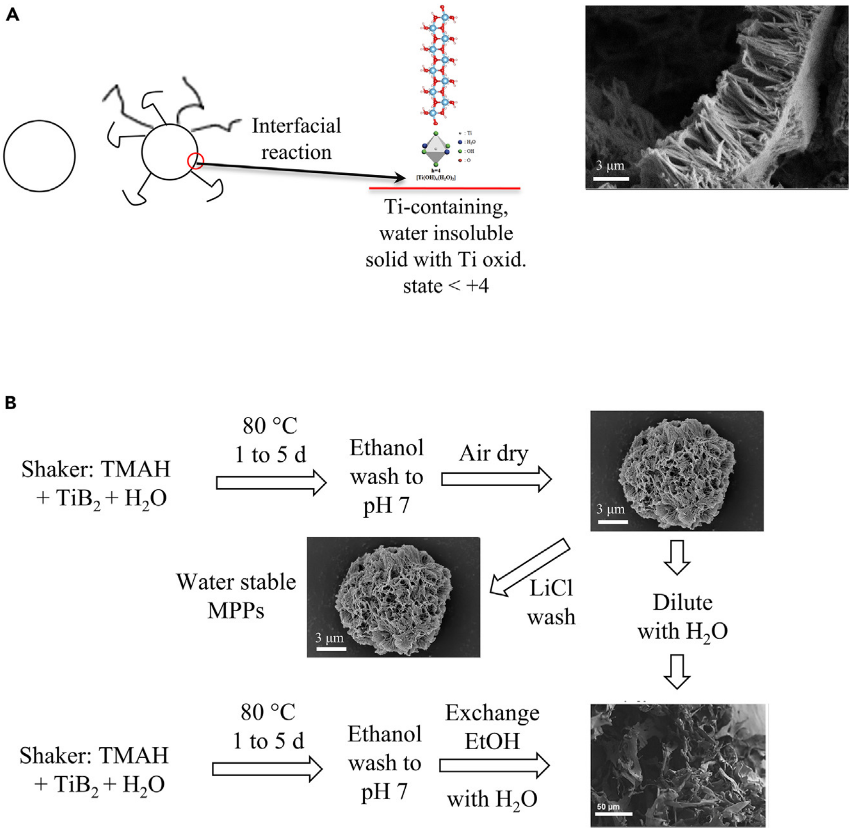

Figure 7. Location of reaction and effects of solvent on morphology

(A) NFs form at the solid/reaction liquid interface by the formation of TiO_6 octahedra and their attachment to the bottom of the growing NF.

(B) Effect of washing procedures on final morphologies. In the absence of water, MPPs form (top row). If water is introduced, quasi-2D sheets are formed (bottom right corner).

Like in our previous work, HR-STEM and SAD patterns confirmed that the building units of the MPPs and quasi-2D sheets are 1D lepidocrocite-type NFs that are 5×7 Å^2 in cross-section and 10's of nm long. The latter self-assemble into nanobundles that, in turn, self-assemble into micron long fibers and, ultimately, either MPPs or quasi-2D layers. SEM micrographs taken as a function of reaction time strongly suggest that the formation of the NF occurs at the TiB_2/reaction liquid interface.

According to our TGA results, the mesoporous morphology is stable up to 800°C. However, the lepidocrocite titania structure transforms into rutile, anatase, and Li- or Na-titanate at temperatures >400°C.

We further investigated the feasibility of intercalating various cations in the interfilamentous gallery. In our first report,[27] we exchanged the TMA cations present after reaction with Li cations. Herein, we show that the NFs are readily ion exchangeable with various monovalent (H_3O^+, Li^+, and Na^+) and divalent cations (Mg^{2+}, Mn^{2+}, Fe^{2+}, Co^{2+}, Ni^{2+}, and Zn^{2+}).

Lastly, we measured the surface charges and hydrodynamic diameters of the self-assembled NFs and showed that the ζ potentials in DI water are in the - 50 mV range, resulting in highly stable colloidal suspensions.

From an industrial perspective, our method is quite simple and scalable. Note that, in this work, neither centrifugation nor filtration was needed in processing the MPPs. This should, in principle, reduce their production cost.

EXPERIMENTAL PROCEDURES

Resource availability

Lead contact

Additional information in this study and requests regarding resources and reagents should be directed to and will be fulfilled by the lead contact, Michel W. Barsoum (barsoumw@drexel.edu).

Materials availability

All information generated in this study is available from the lead contact.

Data and code availability

All data supporting the findings of this study are available within the paper and its supplemental information or from the corresponding authors upon reasonable request. This study did not generate any code.

Materials synthesis and processing

Sample preparation of 1DL

Our scalable synthesis protocol entails mixing commercial TiB_2 (- 325 mesh Thermo Scientific, PA) powders with a TMAH aqueous solution (Alfa Aesar, 25 wt % in DI water, 99.9999%) in polyethylene bottles. The Ti:TMAH mole ratio was kept constant at 0.6. In a typical batch, we immersed 100 g of TiB_2 powder in 900 mL of TMAH aqueous solutions in five different polyethylene bottles, each 250 mL in volume. The bottles were then transferred to a temperature-controlled incubator/shaker (211DS 49L Shaking Incubator, Labnet International, NC) and shaken at 175 rpm at 80°C for 1–5 days.

Washing protocol

After reaction, all the resulting sediment was combined in a 1-L beaker and the powders were allowed to settle, after which the supernatant was decanted and discarded. To wash away any unreacted TMAH, the 1-L beaker was again filled with EtOH (Decon Lab, 200 proof), stirred at room temperature (RT) for 1–2 h using an overhead mixer (OSC-10L-200rpm, LabFish, China), after which the powders were again allowed to settle before the EtOH supernatant, composed of excess TMA^+ cations and other unwanted reaction products, was again dumped to waste. This procedure was repeated multiple times until the pH was ≈ 7, after which the powders were allowed to dry in open air at 50°C overnight.

Synthesis of ion-intercalated 1DL NFs

To assess capability of ion exchange, some powders, while wet, were further stirred on a stir plate three subsequent times each for 6 h in one of the following salt solutions: LiCl 0.5 M, LiCl 5 M, NaCl 0.5 M, or NaCl 5 M. They were then rinsed with DI water three times to remove any unreacted salts and/or reaction products. All salts were purchased from Alfa Aesar with >99% purity. The LiCl- and NaCl-treated powders were then air-dried at 50°C overnight.

X-ray diffraction (XRD)

A diffractometer (Rigaku MiniFlex, Tokyo, Japan) operated with Cu Kα radiation (40 kV and 15 mA) was used to obtained XRD patterns. The powders were scanned in the $2^\circ - 65^\circ$ 2θ range with a step size of 0.02° and a dwell time of 1 s. Unless otherwise noted, all powders were dried overnight at 50°C in open air before any XRD scans.

Scanning electron microscope (SEM)

An SEM (Zeiss Supra 50 VP, Carl Zeiss SMT AG, Oberkochen, Germany) was used to obtain micrographs of our materials. The SEM settings were set to an in-lens detector, a 30-mm aperture, and an accelerating voltage of 3–5 kV.

Particle size distribution

Particle size distribution was carried out by measuring both minimum and maximum lengths of each particle for a total of 100 particles using ImageJ software.

Scanning transmission electron microscope (STEM)

A scanning transmission electron microscope using an aberration-corrected cold field emission JEOL ARM200CF operating at 200-kV primary electron energy was used. Imaging and spectroscopic measurements were conducted with the emission current at 15 μA, an electron probe semi-convergence angle of 24 mrad, as well as inner and outer detector angles of 68 and 280 mrad for high-angle annular dark field (HAADF) imaging. For LAADF imaging, the inner and outer angles were 30 and 120 mrad, respectively. Annular bright field (ABF) imaging was conducted using an outer angle of 23 mrad and an inner angle of 11 mrad.

To conduct nanoscale elemental identification and quantification, the ARM200CF is equipped with an Oxford XMX100TLE X-ray windowless silicon drift detector (SDD) with a 100 mm^2 detector area.[47]

STEM samples were prepared by drop casting a 5-mL suspension of TiB_2-derived powders (5days, 80°C) in methanol on a 3-mm lacey carbon copper grid. The sample was then allowed to dry for an hour before insertion into the microscope column.

Electron energy-loss spectroscopy (EELS)

EELS measurements were conducted using a post-columns Gatan Continuum GIF ER spectrometer, with an electron probe semi-convergence angle of 17.8 mrad and a collection angle of 53.4 mrad. *In situ* cooling was conducted using a Gatan 636 liquid N_2 cold stage. To reduce the presence of latent water, the samples were heated to 100°C for an hour inside the microscope column.

Zeta potential and particle size measurements

A Zetasizer (Nano-ZS, Malvern Panalytical, Malvern, UK) was used for the electrophoretic mobility measurements. The electrophoretic mobility values were converted to ζ potentials using the Smoluchowski model. The hydrodynamic dimaters, d_H was also measured, on the same machine, using dynamic light scattering (DLS). Average d_H was calculated from the diffusion coefficient using the Strokes-Einstein equation. All measurements were carried out at ambient conditions with a holding equilibrium time of 120 s.

Thermogravimetric analysis (TGA)

A thermobalance (TA Instruments Q50, New Castle, DE, USA) was used for the TGA analysis. Dry powders (~40 mg) were loaded in sapphire crucible, heated at 10°C/min, under Ar flow at 10 mL/min to 800°C, then the system was left to cool down naturally.

SUPPLEMENTAL INFORMATION

Supplemental information can be found online at https://doi.org/10.1016/j.matt.2023.07.022.

ACKNOWLEDGMENTS

We would like to thank Mr. A. Walter with help indexing the various XRD patterns. This work was funded by Ceramics Program of DMR of the National Science Foundation, NSF (DMR-2211319) and Murata Manufacturing Co. Ltd. of Japan. R.F.K. acknowledges support from the NSF (DMR-1831406). Acquisition and upgrade of the UIC JEOL JEM ARM200CF was supported by an MRI-R grant (DMR-0959470) and an MRI grant (DMR-1626065) from NSF.

AUTHOR CONTRIBUTIONS

H.O.B. and M.W.B. conceived the idea and supervised all experimental work. H.O.B. wrote the manuscript. J.C. and E.C. prepared all samples. T.K. carried out all ζ-potential and DLS measurements. F.L. and R.F.K. conducted STEM and EELS experiments and analysis. T.T. helped in discussing the results. All authors discussed the results and commented on the manuscript. M.W.B. supervised the project and co-wrote and edited the manuscript.

DECLARATION OF INTERESTS

A provisional patent application entitled "Bottom-Up, Scalable Synthesis Of Oxide-Based Sub-Nano And Nanofilaments And Nanofilament-Based Two-Dimensional Flakes And Mesoporous Powders" naming M.W. Barsoum and H.O. Badr was filed on August 17, 2022.

Received: February 8, 2023
Revised: May 15, 2023
Accepted: July 24, 2023
Published: September 1, 2023

REFERENCES

1. Kumar, S.G., and Devi, L.G. (2011). Review on Modified TiO_2 Photocatalysis under UV/Visible Light: Selected Results and Related Mechanisms on Interfacial Charge Carrier Transfer Dynamics. J. Phys. Chem. A *115*, 13211–13241. https://doi.org/10.1021/jp204364a.
2. Schaub, R., Thostrup, P., Lopez, N., Lægsgaard, E., Stensgaard, I., Nørskov, J.K., and Besenbacher, F. (2001). Oxygen vacancies as active sites for water dissociation on rutile TiO_2 (110). PRL *87*, 266104. https://doi.org/10.1103/PhysRevLett.87.266104.
3. Wang, L., and Sasaki, T. (2014). Titanium Oxide Nanosheets: Graphene Analogues with Versatile Functionalities. Chem. Rev. *114*, 9455–9486.
4. Bourikas, K., Kordulis, C., and Lycourghiotis, A. (2014). Titanium Dioxide (Anatase and Rutile): Surface Chemistry, Liquid–Solid Interface Chemistry, and Scientific Synthesis of Supported Catalysts. Chem. Rev. *114*, 9754–9823. https://doi.org/10.1021/cr300230q.
5. Wang, X., Li, Z., Shi, J., and Yu, Y. (2014). One-dimensional titanium dioxide nanomaterials: nanowires, nanorods, and nanobelts. Chem. Rev. *114*, 9346–9384. https://doi.org/10.1021/cr400633s.
6. Ramos-Delgado, N.A., Gracia-Pinilla, M.Á., Mangalaraja, R.V., O'Shea, K., and Dionysiou, D.D. (2016). Industrial synthesis and characterization of nanophotocatalysts materials: titania. Nanotechnol. Rev. *5*, 467–479. https://doi.org/10.1515/ntrev-2016-0007.
7. Fang, W., Xing, M., and Zhang, J. (2017). Modifications on Reduced Titanium Dioxide Photocatalysts: A review. J. Photochem. Photobiol. C Photochem. Rev. *32*, 21–39. https://doi.org/10.1016/j.jphotochemrev.2017.05.003.
8. Saeed, M., Muneer, M., and Akram, N. (2021). Photocatalysis: an effective tool for photodegradation of dyes—a review. Environ. Sci. Pollut. Res. 1–19. https://doi.org/10.1007/s11356-021-16389-7.
9. Sasaki, T., Watanabe, M., Michiue, Y., Komatsu, Y., Izumi, F., and Takenouchi, S. (1995). Preparation and Acid—Base Properties of a Protonated Titanate with the Lepidocrocite-like Layer. Chem. Mater. *7*, 1001–1007.
10. Sasaki, T., and Watanabe, M. (1997). Semiconductor nanosheet crystallites of quasi-TiO_2 and their optical properties. J. Phys. Chem. B *101*, 10159–10161. https://doi.org/10.1021/jp9727658.
11. Zhou, W., Umezawa, N., Ma, R., Sakai, N., Ebina, Y., Sano, K., Liu, M., Ishida, Y., Aida, T., and Sasaki, T. (2018). Spontaneous Direct Band Gap, High Hole Mobility, and Huge Exciton Energy in Atomic-Thin TiO_2 Nanosheet. Chem. Mater. *30*, 6449–6457. https://doi.org/10.1021/acs.chemmater.8b02792.
12. Lai, Y., Lin, L., Pan, F., Huang, J., Song, R., Huang, Y., Lin, C., Fuchs, H., and Chi, L. (2013). Bioinspired Patterning with Extreme Wettability Contrast on TiO_2 Nanotube Array Surface: A Versatile Platform for Biomedical Applications. Small *9*, 2945–2953. https://doi.org/10.1002/smll.201300187.
13. Hurum, D.C., Agrios, A.G., Gray, K.A., Rajh, T., and Thurnauer, M.C. (2003). Explaining the enhanced photocatalytic activity of Degussa P25 mixed-phase TiO_2 using EPR. J. Phys. Chem. B *107*, 4545–4549.
14. Ohtani, B., Prieto-Mahaney, O., Li, D., and Abe, R. (2010). What is Degussa (Evonik) P25? Crystalline composition analysis, reconstruction from isolated pure particles and photocatalytic activity test. J. Photochem. Photobiol., A *216*, 179–182.
15. Wang, X., Pehkonen, S.O., Rämö, J., Väänänen, M., Highfield, J.G., Laasonen, K., Yang, Q.f., and Ren, Y. (2012). Experimental and computational studies of nitrogen doped Degussa P25 TiO_2: application to visible-light driven photo-oxidation of As (iii). Catal. Sci. Technol. *2*, 784–787.
16. Tobaldi, D.M., Pullar, R.C., Seabra, M.P., and Labrincha, J.A. (2014). Fully quantitative X-ray characterisation of Evonik Aeroxide TiO_2 P25. Mater. Lett. *122*, 345–347.
17. Sheng, L., Liao, T., Kou, L., and Sun, Z. (2017). Single-crystalline ultrathin 2D TiO_2

nanosheets: A bridge towards superior photovoltaic devices. Mater. Today Energy *3*, 32–39. https://doi.org/10.1016/j.mtener.2016.12.004.

18. Esmat, M., Farghali, A.A., El-Dek, S.I., Khedr, M.H., Yamauchi, Y., Bando, Y., Fukata, N., and Ide, Y. (2019). Conversion of a 2D Lepidocrocite-Type Layered Titanate into Its 1D Nanowire Form with Enhancement of Cation Exchange and Photocatalytic Performance. Inorg. Chem. *58*, 7989–7996. https://doi.org/10.1021/acs.inorgchem.9b00722.

19. Badr, H., Natu, V., Neaţu, S., Neaţu, F., Kuncser, A., Rostas, A., Barsoum, M.W., and Florea, M. (2023). Ultra-stable, 1D TiO_2 Lepidocrocite for Photocatalytic Hydrogen Production in Water-Methanol Mixtures. Matter. https://doi.org/10.1016/j.matt.2023.05.026.

20. Badr, H.O., Montazeri, K., El-Melegy, T., Natu, V., Carey, M., Gawas, R., Phan, P., Qian, Q., Li, C.Y., Wiedwald, U., et al. (2022). Scalable, inexpensive, one-pot, facile synthesis of crystalline two-dimensional birnessite flakes. Matter *5*, 2365–2381. https://doi.org/10.1016/j.matt.2022.05.038.

21. Kai, K., Yoshida, Y., Kageyama, H., Saito, G., Ishigaki, T., Furukawa, Y., and Kawamata, J. (2008). Room-Temperature Synthesis of Manganese Oxide Monosheets. J. Am. Chem. Soc. *130*, 15938–15943. https://doi.org/10.1021/ja804503f.

22. Kai, K., Yoshida, Y., Kobayashi, Y., Kageyama, H., and Saito, G. (2012). Preparation and formation mechanism of a n-butylammonium/MnO_2 layered hybrid via a one-pot synthesis under moderate conditions. Dalton Trans. *41*, 825–830.

23. Zhang, A., Zhao, R., Hu, L., Yang, R., Yao, S., Wang, S., Yang, Z., and Yan, Y. (2021). Adjusting the Coordination Environment of Mn Enhances Supercapacitor Performance of MnO_2. Adv. Energy Mater. *11*, 2101412. https://doi.org/10.1002/aenm.202101412.

24. Zheng, W., Halim, J., Yang, L., Badr, H.O., Sun, Z., Persson, P.O.Å., Rosen, J., and Barsoum, M.W. (2022). MXene//MnO_2 Asymmetric Supercapacitors with High Voltages and High Energy Densities. Batteries & Supercaps *5*. https://doi.org/10.1002/batt.202200151.

25. Hassig, M.Q., Kono, T., Carey, M., Sudhakar, K., Schwenk, G.R., Badr, H.O., and Barsoum, M.W. (2023). Reacting Mn_3O_4 powders with quaternary ammonium hydroxides to form two-dimensional birnessite flakes. Ceram. Int. https://doi.org/10.1016/j.ceramint.2023.07.256.

26. Sudhakar, K., Kono, T., El-Melegy, T., Badr, H., Laxmeesha, P.M., Montazeri, K., Semisalova, A., Farle, M., Wiedwald, U., and Barsoum, M.W. (2023). One pot, scalable synthesis of hydroxide derived ferrite magnetic nanoparticles. J. Magn. Magn Mater. *582*, 170986. https://doi.org/10.1016/j.jmmm.2023.170986.

27. Badr, H.O., El-Melegy, T., Carey, M., Natu, V., Hassig, M.Q., Johnson, C., Qian, Q., Li, C.Y., Kushnir, K., Colin-Ulloa, E., et al. (2022). Bottom-up, scalable synthesis of anatase nanofilament-based two-dimensional titanium carbo-oxide flakes. Mater. Today *54*, 8–17. https://doi.org/10.1016/j.mattod.2021.10.033.

28. Badr, H.O., Lagunas, F., Autrey, D.E., Cope, J., Kono, T., Torita, T., Klie, R.F., Hu, Y.-J., and Barsoum, M.W. (2023). On the Structure of One-Dimensional TiO_2 Lepidocrocite. Matter *6*, 128–141. https://doi.org/10.1016/j.matt.2022.10.015.

29. Colin-Ulloa, E., Martin, J.L., Hanna, R.J., Frasch, M.H., Ramthun, R.R., Badr, H.O., Uzarski, J.R., Barsoum, M.W., Grimm, R.L., and Titova, L.V. (2023). Electronic Structure of 1D Lepidocrocite TiO_2 as Revealed by Optical Absorption and Photoelectron Spectroscopy. J. Phys. Chem. C *127*, 7275–7283. https://doi.org/10.1021/acs.jpcc.2c06719.

30. Wang, L., Badr, H.O., Yanga, Y., Cope, J., Ma, E., Yuan, L., Li, Z., Barsoum, M.W., Chai, Z., and Shi, W. (2023). Unique Hierarchical Structures of One Dimensional Lepidocrocite Titanate with Cation-Exchangeable Sites for Extraordinary Selective Actinide Capture for Water Purification. Chem. Eng. J. https://doi.org/10.1016/j.cej.2023.145635.

31. Wilson, O.R., Carey, M.S., Cope, J.H., Badr, H.O., Nantz, J.M., ElMelegy, T.A., Barsoum, M.W., and Magenau, A.J. (2023). Repairable reinforced composites of 1D TiO_2 lepidocrocite mesoparticles and thiol-yne click networks via alkylborane-initiated in situ polymerization. Cell Rep. *4*, 101434. https://doi.org/10.1016/j.xcrp.2023.101434.

32. Sudhakar, K., Karmakar, A., Badr, H.O., El-Melegy, T., Hassig, M.Q., Carey, M., Masiuk, S., Wu, L., Qian, Q., Kono, T., et al. (2023). One-dimensional, Lepidocrocite-based Nanofilaments and Their Self-Assembly. Matter. https://doi.org/10.1016/j.matt.2023.06.006.

33. Ma, R., and Sasaki, T. (2010). Nanosheets of Oxides and Hydroxides: Ultimate 2D Charge-Bearing Functional Crystallites. Adv. Mater. *22*, 5082–5104. https://doi.org/10.1002/adma.201001722.

34. Verger, L., Natu, V., Ghidiu, M., and Barsoum, M.W. (2019). Effect of Cationic Exchange on the Hydration and Swelling Behavior of $Ti_3C_2T_z$ MXene. J. Phys. Chem. C *123*. 20044-20050, 19725-19733.

35. Natu, V., Pai, R., Wilson, O., Gadasu, E., Badr, H., Karmakar, A., Magenau, A.J.D., Kalra, V., and Barsoum, M.W. (2022). Effect of Base/Nucleophile Treatment on Interlayer Ion Intercalation, Surface Terminations, and Osmotic Swelling of $Ti_3C_2T_z$ MXene Multilayers. Chem. Mater. *34*, 678–693.

36. Ma, R., Bando, Y., and Sasaki, T. (2003). Nanotubes of lepidocrocite titanates. Chem. Phys. Lett. *380*, 577–582. https://doi.org/10.1016/j.cplett.2003.09.069.

37. Sasaki, T., Watanabe, M., Hashizume, H., Yamada, H., and Nakazawa, H. (1996). Macromolecule-like Aspects for a Colloidal Suspension of an Exfoliated Titanate. Pairwise Association of Nanosheets and Dynamic Reassembling Process Initiated from It. J. Am. Chem. Soc. *118*, 8329–8335. https://doi.org/10.1021/ja960073b.

38. Yuan, H., Besselink, R., Liao, Z., and Ten Elshof, J.E. (2014). The swelling transition of lepidocrocite-type protonated layered titanates into anatase under hydrothermal treatment. Sci. Rep. *4*, 4584–4610.

39. Tan, Z., Sato, K., and Ohara, S. (2015). Synthesis of layered nanostructured TiO_2 by hydrothermal method. Adv. Powder Technol. *26*, 296–302. https://doi.org/10.1016/j.apt.2014.10.011.

40. Liu, Z.h., Ooi, K., Kanoh, H., Tang, W.p., and Tomida, T. (2000). Swelling and Delamination Behaviors of Birnessite-Type Manganese Oxide by Intercalation of Tetraalkylammonium Ions. Langmuir *16*, 4154–4164. https://doi.org/10.1021/la9913755.

41. Brock, S.L., Sanabria, M., Suib, S.L., Urban, V., Thiyagarajan, P., and Potter, D.I. (1999). Particle Size Control and Self-Assembly Processes in Novel Colloids of Nanocrystalline Manganese Oxide. J. Phys. Chem. B *103*, 7416–7428. https://doi.org/10.1021/jp991009u.

42. Sun, X., and Li, Y. (2003). Synthesis and Characterization of Ion-Exchangeable Titanate Nanotubes. Chem. Eur J. *9*, 2229–2238. https://doi.org/10.1002/chem.200204394.

43. Mao, Y., and Wong, S.S. (2006). Size- and Shape-Dependent Transformation of Nanosized Titanate into Analogous Anatase Titania Nanostructures. J. Am. Chem. Soc. *128*, 8217–8226. https://doi.org/10.1021/ja0607483.

44. Liu, W., Sun, W., Borthwick, A.G., and Ni, J. (2013). Comparison on aggregation and sedimentation of titanium dioxide, titanate nanotubes and titanate nanotubes-TiO_2: Influence of pH, ionic strength and natural organic matter. Colloids Surf. A Physicochem. Eng. Asp. *434*, 319–328. https://doi.org/10.1016/j.colsurfa.2013.05.010.

45. Bavykin, D., Friedrich, J., and Walsh, F. (2006). Protonated Titanates and TiO_2 Nanostructured Materials: Synthesis, Properties, and Applications. Adv. Mater. *18*, 2807–2824. https://doi.org/10.1002/adma.200502696.

46. Yang, J., Jin, Z., Wang, X., Li, W., Zhang, J., Zhang, S., Guo, X., and Zhang, Z. (2003). Study on composition, structure and formation process of nanotube $Na_2Ti_2O_4(OH)_2$. Dalton Trans. *3898*, 3898.

47. Phillips, P.J., Paulauskas, T., Rowlands, N., Nicholls, A.W., Low, K.B., Bhadare, S., and Klie, R.F. (2014). A New Silicon Drift Detector for High Spatial Resolution STEM-XEDS: Performance and Applications. Microsc. Microanal. *20*, 1046–1052. https://doi.org/10.1017/S1431927614001639.